ELSEVIER

Chemical Physics 261 (2000) 205–216

Chemical Physics

www.elsevier.nl/locate/chemphys

# Structure and dynamics from combined neutron scattering and first-principles studies

Taner Yildirim *

*NIST Center for Neutron Research, National Institute of Standards and Technology, Building 235, Room E112, Gaithersburg, MD 20899, USA*

Received 21 March 2000; in final form 22 May 2000

**Abstract**

Using combined first-principles and neutron-scattering techniques, we have studied the structural and dynamical properties of several materials including solid cubane and protonic-conducting oxides. The measured lattice parameters, atomic positions, and vibrational densities-of-states are compared with those obtained from first-principles calculations. In most cases, good agreement was obtained, even for systems as diverse as molecular solids and oxides. In particular, using the van der Waals solid cubane, we tested density functional theory within the local density approximation (LDA) and the generalized gradient approximation (GGA). While calculations within the LDA are in good agreement with the experimental data, GGA calculations predict too large a lattice constant and too small a cohesive energy for solid cubane. © 2000 Published by Elsevier Science B.V.

*Keywords:* Neutron scattering; First-principles methods; Structure and dynamics; Solid cubane; Protonic conductors

## 1. Introduction

In recent years, there has been a growing interest in developing computational models to understand and predict various properties of solids and molecules. Among these, the structural and vibrational properties are probably the most important ones as they determine a wide range of macroscopic behavior such as thermal properties, structural stability and phase transitions. Hence, developing more accurate computational techniques to predict the structural and dynamical properties of materials has become an important research topic. Calculations based on empirical models can handle large systems but suffer a lack of predictive power and accuracy because of the uncertainties in the force-field parameters. On the other hand, calculations based on *first principles* (i.e. density functional theory, DFT, within the local density approximation, LDA) have proven to be very accurate [1]. With today's available computer power, it is now possible to perform realistic simulations in a computer for a system of moderate size (i.e. about 100 atoms per unit cell) using first-principles techniques. Traditionally, these techniques are validated using available experimental structural data such as lattice constants and atomic positions. However such validations are often misleading because of coincidental agreement. On the other hand, comparison of both

* Tel.: +1-301-975-6228; fax: +1-301-921-9847; Web: http://webster.ncnr.nist.gov/staff/taner.

*E-mail address:* taner@nist.gov (T. Yildirim).

0301-0104/00/$ - see front matter 
PII: S0301-0104(00)00231-7

the structure and the dynamics (i.e. the phonon spectrum) to the experimental data is a more stringent test since this requires information about not only the interaction potential but also its second derivatives. Neutron scattering [2] can be used for this purpose since it is one of few techniques which can provide rich information on both structure and dynamics, including the phonon density of states (DOS).

Thermal neutrons are a powerful microscopic probe of condensed matter because their wavelengths are comparable to interatomic distances and their energies are of the same order as typical solid state excitational energies. Thus neutrons may be used to investigate atomic and molecular structures, as well as to probe dynamical phenomena such as molecular rotations [2]. This kind of capability cannot be obtained using other spectroscopic techniques such as Raman and infrared measurements since these methods only probe $\mathbf{q} = 0$ modes, and are subject to selection rules. This sometimes significantly reduces the information that one can measure, particularly for systems with high symmetry. Neutron scattering, however is not subject to selection rules, and can probe excitations in the solid at any momentum transfer $\kappa$.

Calculating an experimental neutron inelastic scattering (NIS) spectrum requires not only the mode energies but also the eigenvectors. The $\mathbf{q}$-dependence of each mode provides more information about the eigenvectors, and can be used to test and validate the first-principles techniques even further. Once the computational techniques are well-tested and validated, they are expected to be highly transferable because of their first-principles nature. Hence, first-principles calculations with its predictive power is an ideal tool to complement and help in the analysis of experimental neutron data.

In this paper we present a brief review of several projects at the NIST Center for Neutron Research that exemplify the power of neutron scattering when combined with first-principles calculations of the structural and dynamical properties of several materials. This paper is organized as follows. In Section 2 we discuss the details of the computational techniques used in the present work. In Section 3 we study the structure and dynamics of solid cubane from first-principles using DFT within both the LDA and GGA. Comparing our results with the available experimental data indicates that LDA works fairly well for solid cubane, while GGA fails. In Section 4, we study the hydrogen dynamics in protonic-conducting oxides using NIS. The data is analyzed by various first-principles frozen-phonon types of calculations. Finally, our conclusions are given in Section 5.

## 2. First-principles calculations and neutron scattering

Total energy and the interatomic force calculations have been performed using the pseudopotential plane-wave code CASTEP [1]. The results have been obtained within the local-density functional approximation (LDA) and using a pseudopotential approach. For solid cubane we also performed calculations within the generalized gradient approximation (GGA) [3] using different cutoff energies, $k$-point samplings, and pseudopotentials to observe the corresponding changes in the results. The electronic wave functions were represented as plane waves with a cutoff energy from 800 to 1500 eV. We used optimized, nonlocal, norm-conserving pseudopotentials in the Kleinman–Bylander form [4] and the Ceperley–Adler exchange-correlation potential [5] in the form parameterized by Perdew and Zunger [6]. Brillouin-zone integrations have been carried out using only the $\Gamma$ point for the large supercells and up to $6 \times 6 \times 6$ $k$-points (according to the Monkhorst–Pack special $k$-point scheme [7]) for small unit cells such as that of solid cubane. Particular values of these parameters are discussed in the following sections separately. The zone-center phonons (i.e. $\mathbf{q} = 0$) are obtained by forming the dynamical matrix. The elements of the dynamical matrix $D_{i\alpha,j\beta}$, are determined by the direct-force method using the supercell geometry. At the zone-center the $\alpha$-component of the Hellmann–Feynmann force on the $i$th ion is calculated by displacing the $j$th ion by $u_\beta \leqslant 0.05$ along $\pm\beta$ directions from its equilibrium position. Accordingly, the dynamical matrix is defined by

$$D_{i\alpha,j\beta} = -\frac{1}{\sqrt{M_i M_j}} \frac{F_{i\alpha}^{+} - F_{i\alpha}^{-}}{u_{j\beta}}, \quad (1)$$

where $F_{i\alpha}^{\pm}$ are the components of the resulting Hellmann–Feynman force exerting on the $i$th ion. By calculating $D$ in this way, we eliminate all force constants that depend on odd powers of the atomic displacements; in particular, the linear and the lowest anharmonic cubic terms have been eliminated. The dynamical matrix, $D$, is then diagonalized to obtain the zone-center vibrational eigenfrequencies of the system under study.

The NIS one-phonon spectrum in neutron-energy loss within the incoherent approximation is calculated from Ref. [2]

$$\frac{d^2\sigma}{d\Omega\, dE} = \frac{k_f}{k_i} \sum_d \frac{\sigma_d}{8\pi} e^{-2W_d(\kappa)} \frac{1}{M_d} \sum_{j\mathbf{q}} |\hat{\kappa} \cdot \hat{\epsilon}_d^j(\mathbf{q})|^2 \times \frac{\kappa^2}{\omega_j(\mathbf{q})} (1 + n_j(\mathbf{q})) \delta(\omega - \omega_j(\mathbf{q})), \quad (2)$$

where $\sigma_d$, $M_d$, and $e^{-2W_d(\kappa)}$ are the total bound scattering cross-section, the mass, and the Debye–Waller amplitude of atom $d$, respectively, and $\epsilon_d^j(\mathbf{q})$ is its eigenvector component with mode energy $\omega_j(\mathbf{q})$. Here, $k_i$ and $k_f$ are the initial and final neutron wavevectors, respectively and $\kappa$ is the neutron-momentum transfer. To the extent that $k_f$ is much smaller than $k_i$ (which is normally the case for the type of spectrometer used in this study), $\kappa^2/\omega_j(\mathbf{q})$ is approximately independent of $\omega_j(\mathbf{q})$. Then the observed intensity in a low-temperature experiment is approximately proportional to the phonon density of states. The averaging of $|\hat{\kappa} \cdot \hat{\epsilon}_d^j(\mathbf{q})|^2$ occurs within the region of $\mathbf{q}$-space sampled by the spectrometer when it is set to detect neutrons whose energy transfer is $\hbar\omega$, and it includes an average over $\mathbf{q}$ if the sample is a powder.

The incoherent approximation used in the above equation is valid for the systems studied here due to the large incoherent neutron cross-section of the hydrogen nucleus. We also use only the zone-center phonons in above equation (i.e. $\mathbf{q} = 0$). This is justified for solid cubane because the molecules are very rigid, and therefore the intermolecular phonons are almost dispersionless. This is also a good approximation for the protonic-conductors because we used a supercell large enough to sample the phonon spectrum.

The NIS measurements reported here were performed using the filter-analyzer spectrometer located on beamline BT4 at the NIST Center for Neutron Research [8]. In most of the measurements, a Cu(2 2 0) monochromator, surrounded by 60′–40′ horizontal collimation and combined with a cooled polycrystalline beryllium filter analyzer was used. The relative energy resolution of this instrument was approximately 8% in the energy range probed.

## 3. Solid cubane

Cubane ($C_8H_8$) [9,10] is a remarkable molecule because of its very rigid cubic cage structure. The C–C–C bond angle is 90° instead of the usual 109.5°; thus cubane is immensely strained, possessing about 6 eV of excess energy. Equally remarkable is the fact that cubane forms a stable solid at room temperature, with a crystalline structure composed of cubane molecules occupying the corners of a rhombohedral primitive unit cell (space group $R\bar{3}$) (see Fig. 1) [11]. The cubic

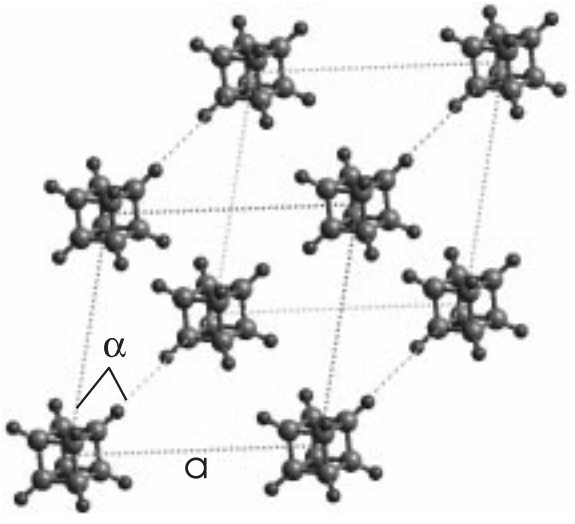


Fig. 1. Crystal structure of solid cubane. For clarity, we set the lattice constant to $a = 10$ Å. Large and small spheres represent the carbon and hydrogen atoms, respectively. Lattice parameters, $a$ and $\alpha$, are also shown.

molecular geometry gives the solid many unusual electronic, structural, and dynamical properties compared to those of other hydrocarbons [9–12, 14–16]. As in many molecular solids, solid cubane undergoes a first-order phase transition ($T_c = 394$ K) from an orientationally ordered phase to a non-cubic orientationally disordered (plastic) phase, resulting in a significant volume expansion of 5.4% [12]. Unlike the cubic plastic phases of many other molecular solids, this phase was found to be also rhombohedral. But it has a different rhombohedral angle, $\alpha = 103.3°$ [12]. The plastic phase persists until $T = 405$ K, at which point cubane melts. Compared to similar size hydrocarbons, the melting point of cubane is very high. The temperature dependence of the properties of solid cubane are also very interesting. It shows a very large thermal expansion, and recent quasielastic neutron scattering along with model calculations indicate very large amplitude orientational dynamics [12,14]. All these indicate that solid cubane forms an ideal model system with which to challenge our understanding of molecular solids, intermolecular interactions, and molecular lattice dynamics.

It is an interesting challenge to predict from first principles some of these unusual properties of solid cubane, which is composed of weakly interacting cubic molecules. Recently we studied the structure and dynamics of solid cubane and its various doped derivatives using DFT within the LDA [16]. We found that DFT within the LDA predicts a lattice constant of $a = 5.07$ Å which is about 5% smaller than the experimental value at 77 K ($a = 5.20$ Å ). Other structural parameters such as the orientation of the cubane molecule and the rhombohedral angle of the unit cell were also found to be in good agreement with the experimental data. However, this agreement raises the question of whether or not it is coincidental because of the van der Waals (vdW) nature of solid cubane. Since vdW interactions are attractive, and missing in the DFT, we expect to obtain a lattice constant larger than the experimental value. This is in contrast to the findings from LDA calculations. Interestingly it is known that DFT within the GGA usually gives larger lattice constants than the corresponding experimental values. Hence it is of interest to compare LDA and GGA calculations for a vdW system like solid cubane. In this section, we will address this issue by studying solid cubane using both LDA and GGA.

The rhombohedral unit cell of solid cubane (see Fig. 1) can be viewed as an face centered cubic (f.c.c.) lattice that has been squashed along one particular [1 1 1] axis. Hence, the structure is characterized by three variables, namely the lattice constant $a$, the rhombohedral angle $\alpha$ (which would be 60° for an f.c.c. structure), and the rotation angle of the molecule about the threefold axis of the cell. We have calculated the total energy of solid cubane as one of these variables is varied while the others are kept constant at the experimental values at 77 K. We have repeated these calculations using different approximations (LDA and GGA), cutoff energies, and $k$-point meshes. The results are shown in Figs. 2 and 3 and compared with the experimental values in Table 1. In all cases, the optimized value of the setting angle (i.e. the orientation) of the cubane molecule is found to be around $\phi = 45°$ ($\phi_{exp} = 46°$), and therefore we will not discuss the dependence of the total energy on this parameter further.

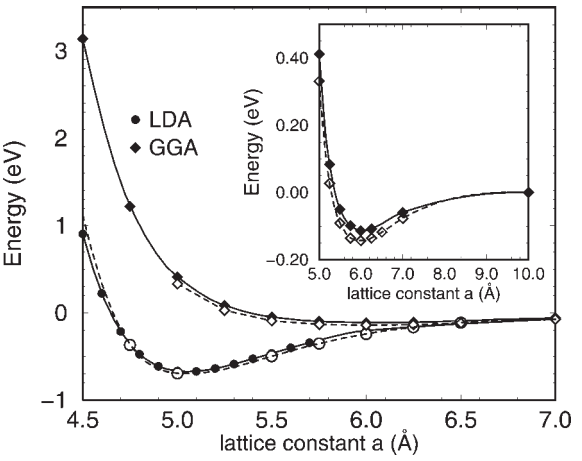


Fig. 2. Total energy of solid cubane versus the lattice constant while other parameters are kept constant at the experimental values. Filled (open) circles and diamonds are the calculated points with $E_{cutoff} = 1500$ eV (1000 eV) and a $k$-point mesh of $6 \times 6 \times 6$ ($5 \times 5 \times 5$). Solid and dotted lines are cubic splines through the calculated points. Inset is an expanded view of the GGA calculations.

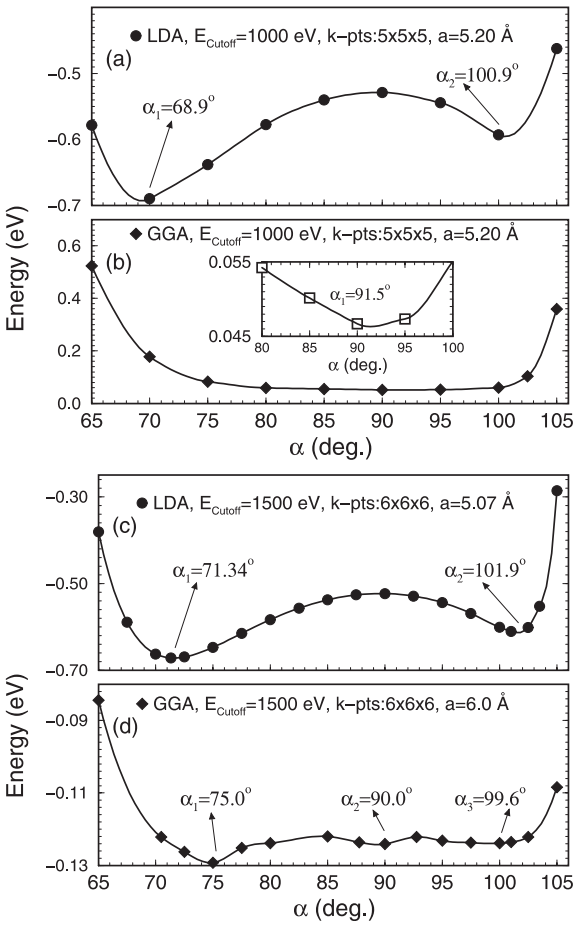


Fig. 3. Variation of the total energy with rhombohedral angle $\alpha$ while the lattice parameter is kept constant at the experimental (a, b) and at the optimized (c, d) values. Points are the calculations, and solid lines are cubic splines.

Fig. 2 shows the lattice constant variation of the total energy calculated with different cutoff energies and $k$-points within the LDA and GGA. Calculations with $E_{\text{cutoff}} = 1500$ eV and $6 \times 6 \times 6$ $k$-points are very similar to the quicker calculation with $E_{\text{cutoff}} = 1000$ eV and $5 \times 5 \times 5$ $k$-points, indicating the convergence of the total energy. However, we see a huge difference between the LDA and GGA calculations. LDA predicts a lattice constant $a = 5.07$ Å and a cohesive energy $E_{\text{coh}} = 0.68$ eV, which are in good agreement with the experimental values [12,13]. On the other hand, GGA predicts a very large lattice constant $a = 6$ Å and a very small cohesive energy $E_{\text{coh}} = 0.11$ eV. We will discuss a possible origin of this disagreement between GGA and LDA later on.

Fig. 3 shows the variation of the potential energy as the rhombohedral angle is varied while the other parameters are kept constant at their experimental (a, b) and calculated optimized values (c, d). For LDA calculations, both sets of cutoff energies and $k$-points gave similar results, indicating one global minimum around 70° and one local minimum around 101°. Interestingly, these values are in good agreement with the experimental values in the orientationally ordered and orientationally disordered phases of solid cubane [12]. Hence LDA calculations with either set of cutoff energies and $k$-points can be considered successful. In contrast, GGA calculations gave very different results depending on the lattice constant used. In the quicker calculation, we do not predict the experimental values for $\alpha$. Instead we obtained $\alpha \sim 90°$, implying a cubic structure. However, we found that this is only true when the lattice constant is fixed at the experimental value $a = 5.20$ Å. We repeated these calculations with $a = 6$ Å using both cutoff energies and $k$-points and obtained very similar results. Fig. 3(d) shows the $\alpha$-dependence of the total energy when the lattice constant is kept constant at the optimized value $a = 6$ Å. It somewhat similar to the results of

Table 1
Experimental structural information for solid cubane and the corresponding optimized values obtained from first-principles calculations using LDA, GGA, and GGA + vdW methods[a]

| Properties | Experiment | LDA | GGA | GGA + vdW |
|---|---|---|---|---|
| $a$ (Å) | 5.20 (at 77 K) | 5.07 | 6.0 | 5.20 |
| $\alpha$ | 72.7° (at 77 K) | 71.3° | 75.0° | 71.4° |
| | 103.3° (at 394.3 K) | 101.9° | 99.6° | 99.9° |
| $E_{\text{coh}}$ (eV) | $0.83 \pm 0.02$ | 0.68 | 0.11 | 0.76 |

[a] Experimental values for the structural parameters and cohesive energy for cubane are taken from Refs. [12,13] respectively.

the LDA calculations. We now predict three minima. The global one is around 75°, and the local ones are around 90° and 100°. Since in the calculations the finite basis set correction [1] was taken into account, the observed changes in the results cannot be attributed to the small changes in the basis set with different lattice constants. Therefore, these results indicate that DFT calculations within the GGA are not well-suited to study the structural properties of solid cubane. However, it is surprising that first-principles calculations within the LDA work so well for solid cubane despite the fact that the system is a vdW solid. This raises a fundamental question: *is the agreement between experiment and LDA a coincidence*?

Since we know that vdW interactions are attractive and not included in the DFT, we naturally expect to obtain a lattice constant that is larger than the experimental value. This is exactly the case for the GGA calculations. By contrast, LDA predicts a smaller lattice constant than the experimental value despite the missing attractive interactions (i.e. vdW) in the theory. The observed agreement between LDA and experiments could be due to one of the following reasons. First, it could be that at the equilibrium structure the overlap of the molecular charge density is large enough that the LDA gives the correct short-range interactions. If this is the case, then the cohesion of solid cubane should be mainly determined by the short-range interactions rather than vdW interactions. The second possibility is that LDA underestimates the short-range repulsive interactions, which accidentally has the same order of magnitude as the missing vdW interactions.

One can study this problem further by calculating the total energy of solid cubane from the GGA plus the vdW interactions. The vdW interactions between atoms $i$ and $j$ can be estimated from the asymptotic limit by the London formula [17]

$$V_{i,j}(\mathrm{vdW}) = -\frac{C_{6ij}}{r_{ij}^6}, \tag{3}$$

where the parameters $C_{6ij}$ are expressed in terms of atomic polarizabilities, $\alpha_i$, and ionization potentials, $I_i$

$$C_{6ij} = \frac{3}{2}\alpha_i\alpha_j\frac{I_iI_j}{I_i + I_j}, \tag{4}$$

where $\alpha_H = 0.42$, $\alpha_C = 0.94$, $I_H = 313.7$, and $I_C = 336.80$ (in units of kcal/mol and Å) [17]. These values are deduced from the empirical atomic refractive indices as used in the additive atomic representations of the molecular refractive indices [17].

Fig. 4 shows the results of such calculations. [1] When the contribution from the vdW is added to the GGA, the total energy has now a minimum at $a = 5.20$ Å and $\alpha = 71.41°$, with a cohesive energy of $E_{coh} = 0.76$ eV. Surprisingly, these values are in excellent agreement with the experimental values measured at 70 K as shown in Table 1. Fig. 4(b) indicates that while the GGA alone does not predict the experimental structure, the GGA + vdW sum predicts both the low-$T$ phase ($\alpha_1$) and the high-$T$ phase ($\alpha_2$) of solid cubane. Remarkably, the resulting variation of the total energy with $\alpha$ is very similar to that obtained from the LDA alone (which is shown in Fig. 3(a)). Hence it is possible that, unlike the LDA, the GGA may describe the short-range interactions accurately, and one needs just the vdW interactions to predict the total energy accurately. Obviously more tests are needed to see if the GGA + vdW method will work for other vdW solids as well as it has for solid cubane. It is also interesting to see if the GGA + vdW method will improve the calculated libron frequencies which are over estimated by GGA. This problem will be studied in the near future.

We next discuss the lattice and molecular dynamics (i.e. phonons and molecular internal vibrations) of solid cubane. Since we have one molecule in the unit cell and since the cubane molecule is composed of $8 + 8 = 16$ atoms, one has $16 \times 3 = 48$ modes. Six of these modes are the external phonons. Three of the six external phonons are acoustic modes, and thus have zero en-

[1] In calculations of the vdW interactions, we used a cutoff distance, $r_{cutoff} = r_{vdW}(H) + r_{vdW}(C) = 1.2 + 1.7 = 2.9$ Å. In order to avoid discontinuities in potential curves, we replaced $V(r_{ij})$ by $V(r_{cutoff})$ when $r_{ij}$ is smaller than $r_{cutoff}$. This problem occurs only for small lattice constants (i.e. $a < 5.0$ Å).

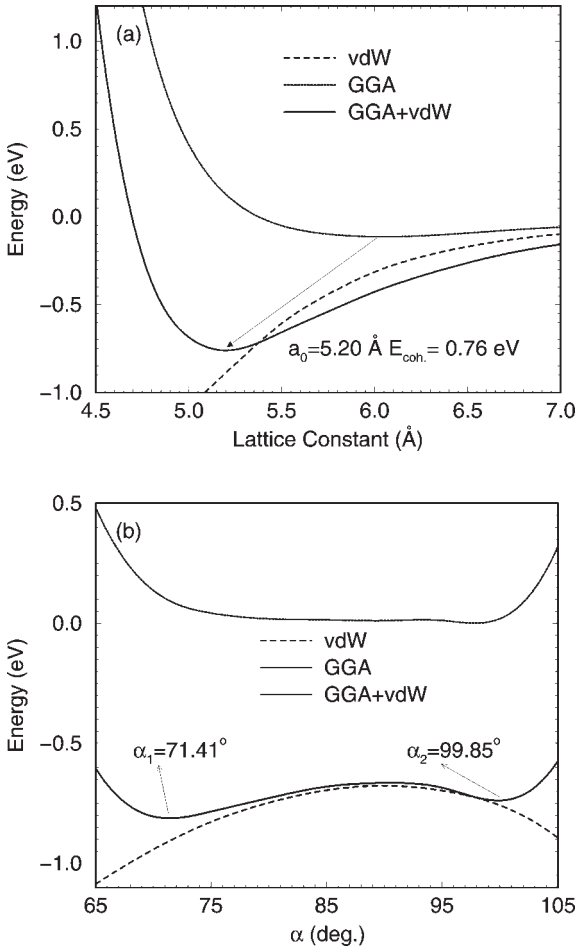


Fig. 4. (a) Contributions from the GGA (···) and van der Waals (- - -) to the total energy (—: GGA + vdW) as the lattice constant is varied while other structural parameters are kept constant. (b) Same as (a) but now for the variation of the total energy with the rhombohedral angle $\alpha$.

ergy since we are calculating the phonons at the zone-center ($\mathbf{q} = 0$). The other three are the librational phonons with one and twofold degeneracies. These correspond to librations of the cubane molecule around the [1 1 1] axis ($A_g$) and the two axes perpendicular to [1 1 1] ($E_g$), respectively. Due to the rigid structure of cubane molecule, the librational modes are well separated from the internal modes in energy. Neutron scattering has already been used to study the phonons and internal modes of solid cubane [15,18,19]. Here we will calculate these modes as described in Section 2

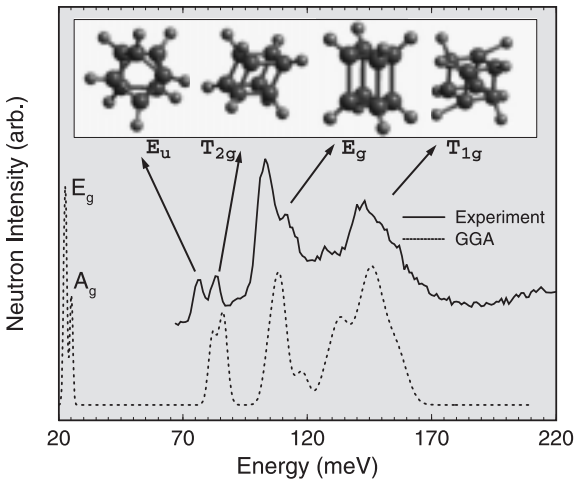


Fig. 5. Neutron spectrum of the vibrational internal modes of cubane (top), and spectrum calculated from first-principles within the GGA (bottom) using measured lattice constants. The inset shows four particular modes identified in the spectrum. The calculated librational modes ($E_g$ and $A_g$) at 26.9 and 31.1 meV are also shown. These values are more than twice the experimental values 11.8 and 14.25 meV at 100 K, respectively.

and make comparison with the experimental data. The phonon calculations were carried out using the experimental lattice parameters at 77 K (but the atomic positions were fully optimized). We used the GGA with $E_{\text{cutoff}} = 1000$ eV, $5 \times 5 \times 5$ $k$-points, and $u = \pm 0.025$ Å for the finite displacements of the atoms. Fig. 5 shows the calculated spectrum along with the neutron data.

The lowest-energy internal mode is observed around 75 meV, which is about six times higher in energy than the highest-energy phonon [18,19]. This demonstrates that cubane molecule is indeed very rigid. The agreement between the data and the calculation is quite good (despite the failure of the GGA to predict the lattice parameters accurately), and allows us to identify the individual modes observed in the spectrum. Some of these modes are shown in the inset.

Fig. 5 also shows the calculated librational modes ($E_g$ and $A_g$) at 26.9 and 31.1 meV, respectively. Even though calculations agree with experiment in that the $A_g$ mode is higher in energy than the $E_g$ mode [15], the calculated mode energies are more than twice the experimental values (measured at 100 K) 11.8 and 14.25 meV, respectively

[18,15]. This is due to the fact that we used the experimental lattice constant $a = 5.20$ Å rather than the optimized value $a = 6.0$ Å. A detailed study of the phonons in solid cubane and their dispersion curves will be published elsewhere.

## 4. Protonic conductors: new materials for fuel cells

Fuel cells have emerged in the last decade as one of the key technologies for meeting the world's energy needs well into the 21st century. Fuel cells are often described as continuously operating batteries or electrochemical engines, which produce electricity by combining hydrogen and oxygen atoms to form water [20]. Because of their chemical (rather than mechanical) nature, fuel cells are safe, highly efficient, nearly silent, and environmentally clean.

Solid-oxide fuel cells (SOFCs) are the most promising among the many different types of fuel cells being developed [20]. However, the required high operating temperature of an SOFC places stringent requirements on its component materials. Potential candidates to replace the oxygen-conducting electrolyte used in current SOFCs include the perovskite-based high-temperature protonic conductors (HTPCs) [21], since switching from anionic to protonic conduction can lower the practical operating temperature from 1300 K to around 1000 K.

The relatively large neutron scattering cross sections for hydrogen renders neutron scattering a useful probe of the proton dynamics and thus the proton conductivity mechanism in these materials. The power of neutron scattering can be further enhanced by first-principles calculations for characterizing the nature of the proton–lattice interactions and associated proton dynamics. In this section, we present various neutron scattering data in conjunction with first-principles total-energy calculations to characterize the proton dynamics in these materials. We hope that such information will help foster the development of new HTPC's with higher proton conductivity.

$SrZrO_3$ and a number of other perovskite oxides are the typical host materials for proton conductors. A view of the structure of undoped $SrZrO_3$ in the [0 0 1] direction is shown in Fig. 6. In these systems one can create oxygen vacancies by doping trivalent ions such as Sc on the Zr sites. The oxygen vacancies can then be filled by exposing the samples to water vapor. The oxygen from the water molecule goes directly into these vacant sites, leaving two protons in interstitial sites. At high temperature, these protons start to diffuse, giving rise to protonic conduction [21] (see Fig. 6). The crystal-structure of $SrZrO_3$ is summarized in Table 2. In the same table, we also give the corresponding theoretical values obtained from our first-principles structure-optimization calculation (using LDA, $E_{\text{cutoff}} = 1200$ eV, and 4 $k$-points), which are in good agreement with the experimental values.

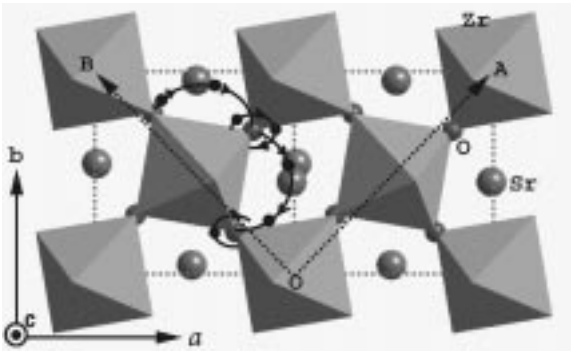


Fig. 6. A view of the structure of undoped $SrZrO_3$ in the [0 0 1] direction. Dotted arrows show the supercell used in the proton dynamics calculations. Dark and gray arrows indicate that protons in the solid can either jump from site to site or rotate around an oxygen ion.

Table 2
Experimental structural information for $SrZrO_3$ (space group Pbnm) and the corresponding optimized values obtained from first-principles calculations (using LDA, $E_{\text{cutoff}} = 1200$ eV, and 4 $k$-points)

| Properties | Experiment | Theory (LDA) |
|---|---|---|
| Cell formula | $Sr_4Zr_4O_{12}$ | $Sr_4Zr_4O_{12}$ |
| $a$ (Å) | 5.786 | 5.738 |
| $b$ (Å) | 5.815 | 5.864 |
| $c$ (Å) | 8.196 | 8.179 |
| Sr(1) | (0.003, 0.526, 0.25) | (0.012, 0.545, 0.25) |
| Zr(1) | (0, 0, 0) | (0, 0, 0) |
| O(1) | (−0.073, −0.018, 0.25) | (−0.105, −0.040, 0.25) |
| O(2) | (0.217, 0.284, 0.035) | (0.207, 0.292, 0.056) |

Recently we undertook neutron vibrational spectroscopy (NVS) measurements of various HTPCs (namely, $SrCeO_3$ and $SrZrO_3$ doped with different rare earth cations) in order to probe the bonding potentials experienced by the residual protons [22]. The NVS measurements reveals the existence of dopant-related perturbations to the bending-mode energies of $OH^-$ species. At high temperatures, these protons migrate from site to site, giving rise to protonic conduction. The NVS measurements revealed the existence of dopant-related perturbations to the bending-mode energies of $OH^-$ in $SrCe_{0.95}M_{0.05}H_xO_{3-\delta}$ (M = Sc, Ho, and Nd), confirming the trapping effects of the dopants. The bending-mode energy could be correlated with the size of the dopant cation, generally increasing for smaller cations. NVS measurements of $SrZr_{0.95}M_{0.05}H_xO_{3-\delta}$ (M = Sc, Y, and Nd) indicated differences in the $OH^-$ bending-mode energies between the cerates and zirconates. These differences reflect changes in the lattice potential experienced by the protons, which ultimately effects the proton jump rates and therefore the performance of these materials for use in fuel cells.

To understand these effects in more detail, here we performed first-principles calculations of the hydrogen dynamics in these systems. Since an understanding of the dynamics of the undoped perovskites is the first step towards a comprehensive picture of the protonated doped materials, we have calculated the $\mathbf{q} = 0$ phonons in the primitive unit cell (i.e. $Zr_4Sr_4O_{12}$) of undoped strontium zirconate and compared it with the experimental DOS at room temperature (see Fig. 7). While at low energies the calculated modes are almost at the same energies as observed modes, at high energies we overestimate the modes by about 10%. However there is still a one-to-one correspondence between the main experimental and calculated spectral features, allowing us to identify the modes. This modest agreement between NVS and calculation suggests that the dispersion of the modes within the primitive cell is not large. We also point out that some of the disagreement between the data and calculations could be due to the fact that experiments were carried out at 295 K while the calculations were for 0 K.

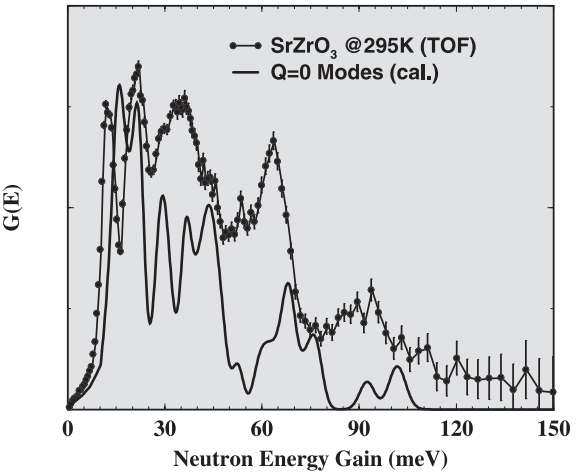


Fig. 7. Vibrational spectra for undoped $SrZrO_3$ measured by neutron time-of-flight spectroscopy. The lower solid line is the DOS of the $\mathbf{q} = 0$ phonons calculated from first-principles. Qualitative agreement between the data and calculation is apparent, which suggests that the dispersion of the phonons in the primitive cell is not large.

In order to model the dynamics of protons trapped in Sc-doped $SrZrO_3$, we replaced one of the Zr atoms in the $\sqrt{2} \times \sqrt{2} \times 1$ supercell (see Fig. 6) by (Sc + H), which yields a cell formula $Sr_8Zr_7ScHO_{24}$. Before calculating the dynamical matrix at the zone center, both the structure and atomic coordinates are fully optimized by the conjugate-gradient method such that the total RMS force on each of the atoms is less than 0.005 eV/Å. In $Sr_8Zr_7ScHO_{24}$, protons can be either at the "undoped" (U) or "doped" (D) sites. We have performed calculations for both cases, and the optimized structures are shown in Fig. 8 (left). Even though the $MO_6$ octahedra are quite rigid, the distortions due to the presence of the proton at these sites are quite large, giving rise to very different vibrational spectra.

Structural and vibrational properties of the H–$MO_6$ (M = Zr and Sc) are compared in Table 3. In both cases, the proton forms an $OH^-$ bond with bond lengths of 0.976 and 1.001 Å at the U and D sites, respectively. While these bond lengths are quite similar, the distance between the proton and the other nearest-neighbor oxygen is quite different: 2.02 Å for the D site and 1.735 Å for the U site. The distance between the proton and the M

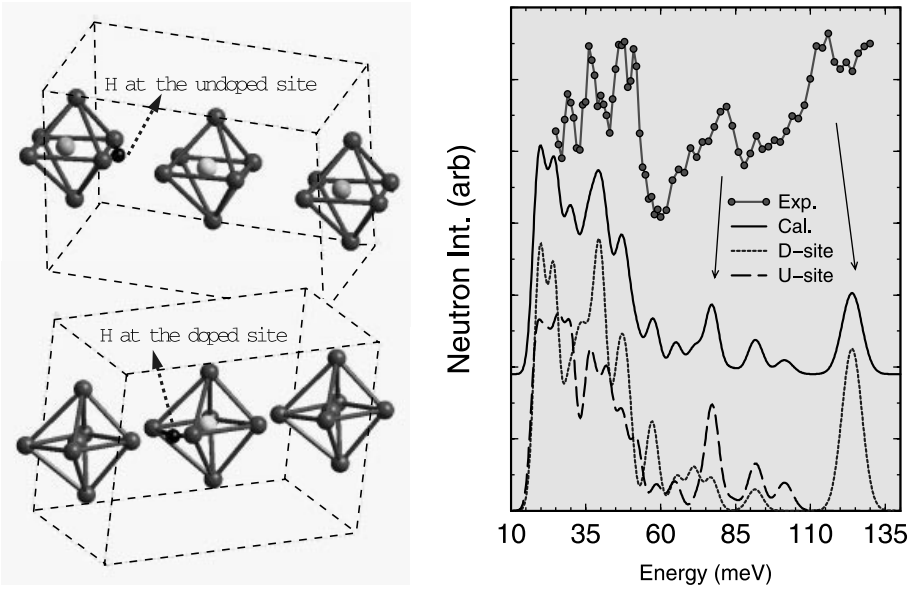


Fig. 8. Left: Optimized structures (some atoms are not shown for clarity) when H is trapped at the undoped site (top) and at the doped site (bottom). Right: Comparison of the neutron vibrational spectrum of $SrCe_{1-x}Sc_xH_xO_3$ with the calculation. Dashed and dotted lines shown at the bottom are the contributions from the H–$MO_6$ clusters where M = Zr (U-site) and M = Sc (D-site), respectively.

cation is much larger for M = Zr (2.359 Å) than for Sc (2.106 Å). This is undoubtedly due to the Coulomb interaction between the proton and the M cation. The large differences in the local geometry of the H–$MO_6$ clusters for M = Zr and Sc are also reflected by the frozen phonon spectrum of the proton. We calculated the vibrational spectrum of the proton assuming all other atoms were at rest in their equilibrium positions. Due to the small mass of the proton, this is expected to be a good approximation. When the proton is at the undoped site, the $OH^-$ stretching mode is at 399 meV. This value is quite similar to the analogous stretching mode in water. However this mode softens significantly to 353.8 meV when the proton is trapped at the doped site.

Table 3
Structural comparison of the equilibrium geometry of the H–$MO_6$ clusters (M = Zr and Sc)[a]

| Properties | U-site ($M = Zr^{+4}$) | D-site ($M = Sc^{+3}$) |
|---|---|---|
| Energy | 0.0 | −1.13 eV |
| $\omega_{O-H}$ | 399 meV | 353.8 meV |
| $\omega_{T_1}$ | 164.8 meV | 157.1 meV |
| $\omega_{T_2}$ | 88.5 meV | 122.9 meV |
| $d_{H-O}$ | 0.976 Å | 1.001 Å |
| $d_{H-O}$ | 2.02 Å | 1.735 Å |
| $a_{O-H-O}$ | 135° | 149.7° |
| $d_{H-M}$ | 2.359 Å | 2.106 Å |

[a] Note that there are large differences depending H is trapped at the M = Zr or M = Sc site.

The two tangential $OH^-$ bending modes are also quite different depending on whether the proton is at the Zr or Sc site. If it is at the Sc site, the lowest tangential mode is found at 122.9 meV. However if it is at the Zr site, the mode is much softer at around 88.5 meV. Interestingly, in the NVS spectrum (top curve in Fig. 8 (right)), we observe features at these energies upon proton addition. To investigate this further, we performed "embedded cluster" calculations in which the vibrational spectrum of only the H–$MO_6$ cluster is calculated while all other atoms are kept at their equilibrium positions. The total spectrum (superposition of the spectra from H–$ZrO_6$ and H–$ScO_6$ clusters) as well as the contributions from individual clusters are shown in Fig. 8 (right). The similarity between experiment and calculation suggests that the mode observed near 120 meV is due protons trapped at the Sc sites while some

portion of the peak near 80 meV is due to free-state protons at the undoped sites.

For a better understanding of the protonic conduction in these materials, it is important to know the diffusion mechanism and relevant energy scales. In particular, we would like to know if the proton at the dopant Sc site has a lower energy than at the Zr site. We calculated the total energy of the system as the proton migrates from Zr to Sc sites, which is shown in Fig. 9. We found that the doped site indeed has a much lower energy (−1.13 eV) than the undoped site. Both sites are separated by an energy barrier of 1.5 eV. Hence, we expect that most of the protons are trapped at the trivalent dopant site if the system is in equilibrium. Since we observed hydrogens trapped at both sites, the system is not in equilibrium. This is most probably due to the large energy barrier between the sites and rapid temperature cooling during the synthesis.

The reason that the trivalent dopant site has a lower energy than Zr site is mainly due to the Coulomb interaction between the proton and the dopant site. Since the cationic charge on Zr is +4, the proton prefers to be closer to Sc, which has a charge of +3. Of course, one has to also consider steric effects. That is, if the dopant cation has a larger radius, then the proton may prefer to occupy the Zr site, despite the larger Coulomb interaction. The competition between the short-range repulsive interaction and this Coulomb interaction can effect the ionic transport. When they are balanced, the proton should no longer have any preference between the Zr and dopant sites, and therefore should not be localized as long at any particular site. This should have the effect of increasing the protonic conductivity. In order to study this more quantitatively, we are currently extending our calculations to different dopant types. Such calculations will be invaluable not only for designing new HTPC's, but also in analyzing quasi-elastic neutron data from which we can obtain detailed information about proton motions.

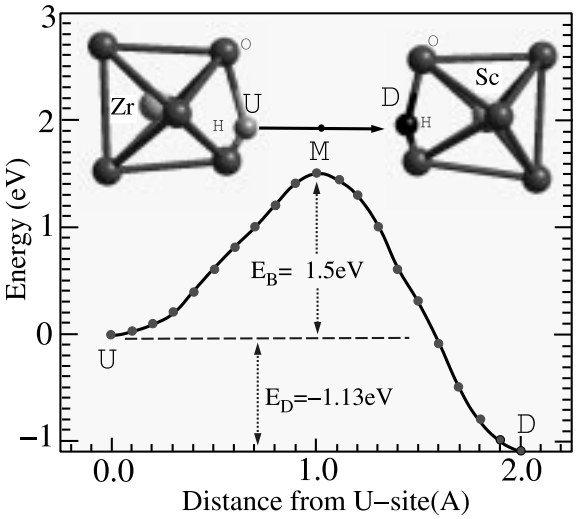


Fig. 9. Potential energy of the crystal as the hydrogen ion migrates from the undoped site (U) to the doped site (D), indicating that the doped site has lower energy by about 1.13 eV than undoped site, which are separated by a potential barrier of about 1.5 eV.

In conclusion, neutron scattering techniques provide a unique means of characterizing the proton dynamics in the HTPC's. Their utility is enhanced by complementary first-principles total-energy calculations, which can be used to help formulate a theoretical-based picture of the mechanisms behind the high protonic conductivities found in these materials. We are currently parameterizing our first-principles calculations by fitting the results (energy and forces) to a potential model. Such a potential will be invaluable in molecular dynamics simulations, which can provide insights concerning the proton dynamics in these materials.

## 5. Conclusion

We have presented a brief review of several projects that demonstrate the power of neutron scattering when combined with first-principles calculations. The work outlined here clearly indicates that we are now at the stage where we can predict structural and dynamical properties of many new materials using first-principles calculations for systems as diverse as molecular solids and oxides. The most difficult task seems to be the prediction of the structural parameters of vdW solids (i.e. solid cubane) from first-principles. Remarkably, the LDA works quite well despite the

fact that the attractive vdW interactions are missing in the theory. Unlike the LDA, the GGA yielded results that are not in good agreement with the experimental data. Interestingly, adding the vdW contributions (estimated from the London formula) to the total energy obtained from the GGA brought the results into excellent agreement with the experimental data. It will be an important computational challenge to determine if the GGA + vdW method will work for other vdW systems as well.

## Acknowledgements

The work reported here was done in collaboration with D.A. Neumann, P.M. Gehring, T.J. Udovic, C. Karmonik, Ç. Kılıç, and S. Ciraci. The author (T.Y.) acknowledges the support of the National Institute of Standards and Technology, US Department of Commerce, in providing the neutron facilities used in this work. T.Y. also acknowledges partial support for the cubane study from the National Science Foundation under Grant no. INT97-31014.

## References

[1] M.C. Payne, M.P. Teter, D.C. Arias, J.D. Joannopoulos, Rev. Mod. Phys. 64 (1992) 1045.
[2] S. Lovesey, Theory of Neutron Scattering from Condensed Matter, third ed., Oxford University Press, New York, 1987.
[3] J.P. Perdew, Y. Wang, Phys. Rev. B 46 (1992) 6671.
[4] L. Kleinman, D.M. Bylander, Phys. Rev. B 48 (1982) 1425.
[5] D.M. Ceperley, B.J. Alder, Phys. Rev. Lett. 45 (1980) 556.
[6] J.P. Perdew, A. Zunger, Phys. Rev. B 23 (1981) 5048.
[7] H. Monkhorst, J.D. Pack, Phys. Rev. B 13 (1976) 588.
[8] J.R.D. Copley, D.A. Neumann, W.A. Kamitakahara, Can. J. Phys. 73 (1995) 763.
[9] P.E. Eaton, T.W. Cole Jr., J. Am. Chem. Soc. 86 (1964) 962.
[10] P.E. Eaton, Angew. Chem. 31 (1992) 1421.
[11] E.B. Fleischer, J. Am. Chem. Soc. 86 (1964) 3889.
[12] T. Yildirim, P.M. Gehring, D.A. Neumann, P.E. Eaton, T. Emrick, Phys. Rev. Lett. 78 (1997) 4938.
[13] B.D. Kybett, S. Carroll, P. Natale, D.W. Bonnell, J.L. Margrave, J.L. Franklin, J. Am. Chem. Soc. 88 (1966) 626.
[14] T. Yildirim, P.M. Gehring, D.A. Neumann, P.E. Eaton, T. Emrick, Phys. Rev. B 60 (1999) 314.
[15] T. Yildirim, P.M. Gehring, D.A. Neumann, P.E. Eaton, T. Emrick, Carbon 36 (1998) 809.
[16] T. Yildirim, S. Ciraci, Ç. Kılıç, A. Buldum, Phys. Rev B (2000) in press.
[17] A.J. Pertsin, A.I. Kitaigorodsky, The Atom–Atom Potential Method: Applications to Organic Molecular Solids, in: V.I. Goldanskii, F.P. Schafer, J.P. Toennies (Eds.), Springer Series in Chemical Physics, vol. 45, 1986.
[18] P.M. Gehring, D.A. Neumann, W.A. Kamitakahara, J.J. Rush, P.E. Eaton, D.P. VanMeurs, J. Phys. Chem. 99 (1995) 4429.
[19] T. Yildirim, Ç. Kılıç, S. Ciraci, P.M. Gehring, D.A. Neumann, P.E. Eaton, T. Emrick, Chem. Phys. Lett. 309 (1999) 234.
[20] K. Kordesch, G. Simader, Feul Cells and Their Applications, Weinheim, New York, 1999.
[21] P. Colomban (Ed.), Proton Conductors, Cambridge University Press, Cambridge, 1992.
[22] C. Karmonik, T. Yildirim, T.J. Udovic, J.J. Rush, R. Hempelmann, Mat. Res. Soc. Symp. Proc. 496 (1998) 199.